Geysers, boiling groundwater and tectonics: the 3D subsurface resistive structure of the Haukadalur hydrothermal field, Iceland

Matteo Lupi[1], Marine Collignon[1], Federico Fischanger[2], Aurore Carrier[1,3], Daniele Trippanera[4], and Laura Pioli[1,5]

[1]Department of Earth Sciences, University of Geneva, Switzerland.

[3]ADRGT, Grenoble, France

[2]Geostudi Astier, S.r.l., Livorno, Italy

[4]Department of Earth Sciences and Engineering, King Abdullah University of Science and Technology (KAUST), Saudi Arabia

[5]Department of Chemical and Geological Sciences, University of Cagliari, Italy

Key Points:

- 3D resistive structure of the geyser-hosting Haukadalur hydrothermal field;
- Vapour-saturated boiling reservoirs feeding geysers and hydrothermal ponds;
- Fluid flow controlled by local tectonics.

Corresponding author: Matteo Lupi, Matteo.Lupi@unige.ch

Abstract

Geysers are among the most fascinating geological features on Earth. Yet, little is still known about their hydrogeological structure at depth. To shed light on the spatial relationships between the vertical conduits and the aquifers feeding them, we conducted a 3D geoelectrical campaign in the Haukadalur hydrothermal field, Iceland. We deployed 24 Iris Fullwavers across the hydrothermal field and inverted resistivity and chargeability measurements. Additionally, we measured temperature variations inside Strokkur and Great Geysir geysers showing temperature fluctuations pointing out the oscillatory behaviour that characterises the geysering cycle of the geysers. By combining a semi-quantitative temperature distribution of the thermal springs across the hydrothermal field with the inversion of the geoelectrical data, we highlight the control that extensional tectonics have on the distribution of fluids across the hydrothermal field. We also point out the occurrence of a common deep groundwater reservoir feeding the hydrothermal centres. Induced polarization data show that the geysers are fed by sub-vertical water-filled fracture zones. The geysers are found at the margins of highly resistive regions where we speculate boiling groundwater and vapour is found. Our proposed model suggests that local waters feeding the main groundwater reservoir downwell from the nearby region and then convect upwards, phase transitioning into vapour at about 200 m depth. From here, fluids flow towards the surface through pipes cutting a highly pressurised and hot system. This study shows to the best of our knowledge the first full 3D tomographic image of a hydrothermal field hosting geysers.

1 Plain Language Summary

Geysers are among the most fascinating geological features on Earth. Yet, little is still known about their hydrogeological structure at depth. To shed light on the spatial relationships between the vertical conduits and the aquifers feeding them, we conducted a 3D geoelectrical campaign in the Haukadalur hydrothermal field, Iceland. We deployed 24 gps-synchronised voltmeters across the hydrothermal field to record the changes of the potential field promoted by the injection of current. This allowed us to characterise the resistivity of the geological units and reconstruct the geological structure at depth. Additionally, we lowered thermometers inside Strokkur and Great Geysir geysers showing temperature fluctuations. We also mapped the temperature of the springs of the Haukadalur hydrothermal field thanks to a thermal camera mounted on a drone. This multidisciplinary dataset allowed us to highlight the control that extensional tectonics have on the distribution of fluids across the hydrothermal field. We also point out the occurrence of a common deep groundwater reservoir feeding the hydrothermal centres. The geysers are found at the margins of gas-rich regions where we speculate boiling groundwater and vapour are found. Our proposed model suggests that local waters feeding the main groundwater reservoir percolate from the nearby region and then convect upwards, phase transitioning into vapour at about 200 m depth. From here, fluids flow towards the surface through pipes cutting a highly pressurised and hot system. This study shows to the best of our knowledge the first full 3D tomographic image of a hydrothermal field hosting geysers.

2 Introduction

Geysering is characterised by the periodic eruption of water driven by a phase transition from liquid to vapour. Being in thermodynamic equilibrium around the phase transition of water, geysering systems are sensitive to external forcing and transient variations of pressure (Husen et al., 2004; Hurwitz et al., 2008). Jet heights, eruptive intervals and lasting of the eruptions may vary over time. Despite being a fascinating phenomenon, little is still understood about the charging and discharging cycles of geysers because of the complex morphology of the pipes and the intricate fracture networks feeding them. Several models have been proposed to explain the processes leading to the eruptions. Early studies proposed that eruptions are driven by increasing pressure due to exsolution of steam trapped in an underground cavity (MacKenzie, 1811). Years later Bunsen (1847) proposed that eruptions may be caused by the exsolution of vapour in an upwelling groundwater column due to the decompression. More recent studies proposed that geysers are fed by single fracture-like conduits (O'Hara & Esawi, 2013; Namiki et al., 2014; Munoz-Saez et al., 2015). Field data suggest the possible occurrence of a lateral cavity, named 'bubble trap', where exsolved volatiles accumulate and pressure builds up (Cros et al., 2011; Vandemeulebrouck et al., 2013, 2014; Belousov et al., 2013; Ardid et al., 2019). Laboratory experiments (Adelstein et al., 2014; Rudolph & Sohn, 2017; Rudolph et al., 2018a) provided further insights on geysers dynamics investigating their oscillatory behaviour. In particular, Rudolph et al. (2018b) tested the geysering behaviour in case the gas behaves as an ideal isothermal gas or as isenthalpic steam. Recent studies suggest that CO_2 and N_2 play key roles in controlling eruptive geyser dynamics (Hurwitz et al., 2016; Belousov et al., 2013; Ladd & Ryan, 2016). However, while laboratory helped to constrain the physical behaviour of the plumbing systems, little is still known about the subsurface shallow geology and the spatial relationships of the aquifers feeding active geysers.

The Haukadalur hydrothermal field (Hhf), Iceland, is found at about 100 m a.s.l. and hosts fumaroles, hydrothermal ponds and active geysers, the most famous of which are the Great Geysir and Strokkur. It develops along a NE-SW direction, subparallel to the strike of the major fault structures of this region (Walter et al., 2018). Recent relocated earthquakes show right-lateral strike-slip to transtensional shallow deformation (Thorbjarnardóttir et al., 2020). The Hhf hosts about 360 hydrothermal emission centres including hot springs, fumaroles and the two geysers Strokkur and Great Geysir Walter2018 (see also Figure 1). The Great Geysir and Strokkur are erupting at different time intervals. Strokkur (that was drilled in 1963 (Walter et al., 2018)) erupts regularly, with eruptions occurring every 5 to 7 minutes (on average) producing jets about 30 m high. The Great Geysir erupts less regularly averaging to about an eruption per year producing jets that have reached in the past about 80 m high (Walter et al., 2018). Eibl et al. (2021) propose that for Strokkur a single-bubble trap model is more suitable than a multiple bubble trap model. The hydrothermal springs and fumaroles formed sinter deposits at least since the 1104-1158 AD (Jones et al., 2007). Lavas were interpreted as sills intruded at depth and in the topographic heights that bound the Hhf on the North-West. It is suggested that Strokkur and Great Geysir geysers develop along vertical fracture-like pipes reaching at least 20 m depth (Pasvanoglu et al., 1998; Torfason & Davíðsson, 1985; Walter et al., 2018). Yet, besides indirect geophysical studies (e.g. Eibl et

al. (2020) and Eibl et al. (2021)) little is known about the plumbing system at depth. Pasvanoglu et al. (1998) propose that the ground water system of *Hhf* is recharged by meteoric waters flowing from the Langjöokull ice-sheet to the North. A marked geochemical evidence shows that locally the groundwaters interacted with acid magmatic units in the *Hhf* (Pasvanoglu et al., 1998).

Electrical resistivity is a method often used in hydrogeophysics (e.g. (Pollock & Cirpka, 2012)) and more recently tested to investigate shallow geothermal systems (Gresse et al., 2017; Carrier et al., 2019; Mazzini et al., 2021). Traditional geoelectrical cabled hardware requires logistically complex operations and 3D acquisitions are performed thanks to interpolated 2D geoelectrical profiles (e.g. Revil et al. (2010)). Large prospection depths can be attained by using remote electrodes that require several kilometers of cable (e.g. Pucci et al. (2016)). ®IRIS has recently released the Fullwaver hardware that allows the acquisition of 3D geoelectrical datasets by scattering independent GPS-synchronised volt-meters across the investigated region (e.g. Carrier et al. (2019); Lajaunie et al. (2019); Sapia et al. (2021); Mazzini et al. (2021)). Despite the inaccessibility of certain areas (i.e. in close proximity to the sinter deposits surrounding the geysers' vents) in June 2018 we deployed the Fullwaver system in the *Hhf* acquiring resistivity and chargeability data (Figure 2). This study presents the geoelectrical and temperature that allowed us to propose the geological model of the *Hhf*.

3 Methods

3.1 Geoelectrical data acquisition and processing

The ®IRIS Instruments Fullwaver system is a quasi-cable less technology that allows the prospection of logistically complex settings with geoelectrical methods. The system can be coupled with high power transmitters and allows recording full-waveform measurements with a 100 Hz sampling rate for both I_{AB} injected currents and V_{MN} received potentials (Carrier et al., 2019; Lajaunie et al., 2019). On June 2018 we deployed a set of 24 Fullwaver devices across the *Hhf* to complete a full 3D survey of the area (Figure 1). The month of June was specifically selected as the continuous light allowed us to work after dawn avoiding the tourist crowds visiting the site. We used an ®Iris Instruments VIP 5000 transmitter, designed to inject a precisely regulated time domain waveform current into the ground up to 10 A, 24 V-Fullwavers (receiving nodes) and one I-Fullwaver box (injection node). Each receiving node records the data acquired by three electrodes, i.e. two dipoles deployed as shown in Figure 2 (red inverted triangles). The layout of the electrodes has been constrained by the accessibility of the area (i.e. presence of the hydrothermal structures) so the sensors were arranged according to an irregular geometry. We spread the 24 receivers over an area large enough to allow an extensive investigation of the hydrothermal field, placing the two main structures, Great Geysir and Strokkur (Figure 2), in the central part of the investigated region. The dipole length for the receivers was derived from a preliminary survey design where we modelled the expected V_{MN} signals for a conductive scenario (which later turned out to be around 30 Ohm.m) combined with the assumption of injecting currents thresholds around 3-5 Amps. This modeling led to select 50 m length dipoles in the central part of the survey area and 100 m dipoles at the margins of the

¹¹⁹ network. This granted a higher resolution in the centre of the network and a broader coverage on the sides. Due ¹²⁰ to the marked 3D geological framework of the survey area, we decided to arrange the dipoles with an L-shaped ¹²¹ configuration, when logistically possible, to achieve a full three-dimensional sensitivity of the final dataset.

¹²² In total, 23 transmitting electrodes (yellow triangles in Figure 2) and 33 dipole combinations were imple-¹²³ mented. The transmitters/receivers combinations have led to both pole-dipole (one 'remote' transmitter and ¹²⁴ one close to the receiver) and dipole-dipole arrays (small innermost dipoles) plus gradient-type measurements ¹²⁵ (largest dipoles). The largest distance between the transmitting electrodes was about 2 km along a NE-SW ¹²⁶ direction (Figure 1). We were able to inject into the ground between 2 and 6 Amps, using a 2 sec OnTime/2 ¹²⁷ sec OffTime waveform with around 3 minutes duration per transmission. These long-lasting injections allowed ¹²⁸ us to stack the signal minimising the effects of possible electromagnetic noise, and eventually compensating the ¹²⁹ (expected) locally high conductivity of the shallow subsurface (the *Hhf* is bounded by a river and the water ¹³⁰ table almost reach the surface). The full dataset consists of 1584 quadrupole measurements. All the electrodes ¹³¹ have been surveyed with a high precision differential GNSS device. Errors on the position of the sensors are ¹³² below 2 m. Site topography to accurately model the terrain was extracted from the *USGS EarthExplorer*[1] ¹³³ platform.

¹³⁴

¹³⁵ Data processing required a preliminary step to check the consistency of the polarities at receiving dipoles, in ¹³⁶ order to correct possible electrode swaps and mistakes during deployment. Also, any transmitter-to-receiver out-¹³⁷ of-synch issue due to the lost of the GPS signal was carefully investigated and fixed. The recorded potentials are ¹³⁸ characterized by clean signals, with average values of 1 mV and maximum values around 500-600 mV. The final ¹³⁹ set of apparent resistivities and chargeabilities to process was achieved through the *Fullwave Viewer* software[2], ¹⁴⁰ which combines the V_{MN} potentials for each V-Fullwaver box with the I_{AB} current for each transmission. Before ¹⁴¹ running the resistivity inversion, 24 quadrupoles with low signal amplitude, below 0.05 mV, were removed from ¹⁴² the dataset. These measurements were related to combinations of small transmitting dipoles far from the ¹⁴³ receivers. The average of apparent resistivities for the dataset is around 28 Ohm.m and confirms the conductive ¹⁴⁴ environment postulated during the planning of the campaign. Induced polarization (IP) measurements were ¹⁴⁵ derived by performing an arithmetic sampling of each time domain decay curve, setting a delay time of 240 ¹⁴⁶ ms and averaging the integral of the curve over 20 consecutive windows of 80 ms each. About 100 further ¹⁴⁷ measurements were removed from the set for the sole chargeability inversion. These were characterized by ¹⁴⁸ high standard deviations (>20%) as calculated on the different stacks, plus a few negative IP values. The ¹⁴⁹ average of the standard deviations after the removal of inaccurate measurements is around 2% and the range ¹⁵⁰ of variation of the IP is 0.1-30 mV/V with an average of 6-7 mV/V. Histograms with statistic distribution ¹⁵¹ of the data are shown in Figure 3. These filtered dataset were processed with the *ERTLab Studio*[3] software

---

[1] https://earthexplorer.usgs.gov/

[2] http://www.iris-instruments.com

[3] http://www.geostudiastier.it/area_en.asp?idCanale=56&sezione=1

152   (Morelli & LaBrecque, 1996; Sapia et al., 2021). We adopted a 15 m size for the three-dimensional finite

153   elements mesh in each direction. The depth of investigation was set to 300 meters. The theoretical sensitivity

154   (see supplemental online material) for the deeper quadrupoles in *ERTLab Studio* considers that the median z

155   depth is calculated so that the area under the sensitivity curve is equal to the 50% of the total area (Barker,

156   1989). Several inversion tests were performed to better explore the models space that fit the measurements.

157   We set the starting homogeneous background resistivity at values ranging from 10 Ohm.m to 100 Ohm.m and

158   tested both isotropic and anisotropic constraints for the model vertical and lateral roughness. We did not

159   notice dramatic changes in the main features retrieved by the different inversions. We therefore present the

160   inversion that accounted for a background of 50 Ohm.m (resistivity) and 7 mV/V (chargeability) and "isotropic"

161   roughness conditions. Gaussian noise on data was estimated to 2% and 5% respectively for resistivity and IP

162   measurements. Resistivity inversion converged in 8 iterations with a final chi-squared statistics of 1241 (inverted

163   measurements are 1562), IP inversion converged in 7 iterations with a final chi-squared statistics of 1167 (vs 1427

164   inverted data-points). For each V/I and IP measurement, (Fullwaver) data are recorded on multiple stacks,

165   normally about 45 repetitions per data-point during about 180s long transmissions. This allows estimating

166   data noise in terms of standard deviations. After removing bad measurements, we found that the average of

167   standard deviations is around 2% for the V/I measurements and 5% for the IP data. We used these values to

168   run resistivity and chargeability inversions. Considering each V/I (or IP measurement) as the realization of a

169   random process and assuming that every data-point d_j for j = 1, 2, ..., ND has a known variance σ_j^2, the ability

170   of the inverted model to adapt to the data is quantified by the following 2-norm function:

171   $$X^2 = \| \ W \ [d - d\_mod] \ \|_2^2.$$

172   Where: d_mod is the set of synthetic measurements that derive from the recovered model (see also addi-

173   tional figures in the supplemental online material). The matrix W can be expressed as a diagonal matrix ND x

174   ND given by W = diag 1 / σ_1, 1 / σ_2,..., 1 / σ_{ND}.

175   The lower is X^2, the higher is the fit. However, the fit should be subject to a statistically reasonable

176   tolerance because of the of noise on data. Assuming that the error on the data is uncorrelated and due to a zero

177   mean Gaussian process, then X^2 is a chi-squared distribution with an expected value equal to ND, the number

178   of independent data. Generally, we consider a model over-fitted when X^2 is strongly lower than ND ($X^2 \ll$ ND,

179   the model is fitting noise and artifacts appear) and an under-fitted – smooth – model is associated to X2 $\gg$

180   ND. In both our inversions our final X^2 is lower than ND within a range of 20%. This slight over-fitting of the

181   data may still be considered reasonable because of the on the standard deviations estimate and because of the

182   presence of non-Gaussian noise in the real world.

183   In Figure 3 we report the data cross-plots that show a good fit between measured and modelled data at

184   the end of the inversions. Outliers are associated to higher standard deviations.

3.2 Temperature data acquisition

The semi-quantitative measurement of the temperatures of the springs and hot ponds have been acquired with a flir thermal camera (Flir Duo R, equipped with a 160 x 120 IR sensor) mounted on a quadricopter (DJI Phantom 4 Pro). Images were calibrated on topography against photogrammetrical reconstruction based on optical images collected from the same drone with a 20 Mp optical camera. The drone flew at an altitude of 65 m above the ground collecting 417 pictures with 75% of both front and side overlap. We placed and measured with a kinematic GPS 10 markers to reduce the error of the reconstruction. After the Structure from Motion processing by using Agisoft Metashape, we finally obtained an orthomosaic with a resolution of 1.6 cm/px and a DTSM of 3.2 cm/px (Figure 1). The measurements were acquired to retrieve the relative variation of temperature across the *Hhf*. Absolute temperature measurements have been acquired by lowering 5 HOBO U12 data loggers into Strokkur and the Great Geysir. We lowered 3 data-loggers inside Strokkur at 9 m, 16 m, and 25 m inside the conduit. The deeper data-logger could not withstand the pressure and temperature conditions encountered at depth and failed. The data-logger was repeatedly sucked in and stuck at depth in multiple occasions. Unlocking of the data-logger was only possible after major eruptions of Strokkur. Visual inspection has shown deep-scratches on the metallic body of the sensor (such scratches did not occur on the shallower data-loggers) suggesting that the sensor may have been stuck in narrow fracture-like channels that were larger than the diameter of the cylindrical datalogger (i.e. 2 cm). We also lowered two temperature data-loggers inside the Great Geysir at 5 m and 10 m depth and no problems were encountered.

4 Results

The *Hhf* is characterised by marked contrasts of resistivity and chargeability (Figure 4). It is possible to recognise a highly conductive and a highly resistive domain separated by a well-defined sharp transition running along a North-North East direction. Figure 4a,b highlight that the most prominent hydrothermal manifestations are associated to highly resistive bodies. For instance, the Great Geysir is found to occur above a moderately resistive region (about 350 Ohm.m). Strokkur occurs at the sharp limit between a highly resistive (more than 1000 Ohm.m) and a highly conductive domain. With increasing depth, the transition between resistive and conductive values is less marked. However, below Strokkur at 0 m a.s.l., i.e. at 100 m depth (Figure 4c) the resistive values are still higher (about 800 Ohm.m) than the surrounding rocks. Similarly, the region below the hydrothermal pond of Littli Geysir (see Figure 1 for its approximate position) that is occasionally erupting with intense bubbling (jets reach less than 50 cm high), is marked by high resistive values until at least 100 m depth (i.e. 0 m a.s.l.), see Figure 4c. At 150 m below the ground surface (Figure 4e) the contrast between resistive and conductive regions is less pronounced. However, the *Hhf* is characterised by higher resistive values elongated according to a direction ∼N23 (note that the panels of Figure 4 are rotated with regards to the North).

The inversion of the IP data allowed us to create the chargeability map of the *Hhf* (Figure 4f-l). At shallow depths all the major hydrothermal features (with possibly the exception of Konungshver) fall within regions characterised by no chargeability (Figure 4f). The prospected region is marked by low chargeability

values towards the East while higher chargeability values occur in the Western region, i.e. in the surroundings of the topographic relief. At greater depths (i.e. at 0 m below the ground, Figure 4h) the chargeable units are quasi-continuous and occur to the West of the main hydrothermal features of the *Hhf*. The limit between chargeable and non-chargeable regions is well-defined and strikes NNE-SSW.

Figure 5 shows that the resistive regions depart from the North-Western side of the surveyed region and dip towards the South-East. The inversion of the resistive data show the occurrence of vertical resistive domains immediately below the major hydrothermal features of the *Hhf*. In particular, Figure 5a highlights that below Strokkur, it is located a shallow, highly-resistive region culminating in the shallow subsurface. The resistive values, below the Great Geysir, although present, are less prominent. The cross section running North-South (Figure 5e) points out the depth of the main resistive body and the relative spatial distribution of the hydrothermal emission centres. The base of the resistive body is found at about 150 m depth and its lateral extent is approximately 500 m in both the North-South and East-West directions.

The chargeability data show that the geysers Strokkur and Great Geysir lay above sub-vertical regions of no chargeability (Figure 5b, d, and f). Similarly, all the major hydrothermal emission centres (e.g. Litli Strokkur and Konungshver) seem to show a similar hydrogeological setting. While domains characterised by conductive values well-match regions characterised by negligible to no chargeability, regions marked by high resistive values do not correspond to regions featuring high chargeability. All the cross-sections show that regions with no chargeability reach about 100 m depth.

4.1 Thermal analyses

Surface measurements highlighted the occurrence of 110 ponds of hot water, and 122 hot spots (i.e. herein defined as isolated and confined emissions marked by increased temperature compared to the surroundings) distributed over the entire area and highlighted by lack of vegetation, but mostly concentrated in its southern and northern portions, along a SSE-NNE and SE-NE alignments (Figure 1). Water in the ponds had temperature ranging from 20°C to 85° whereas hot spots showed temperatures ranging from 15°C to 69°.

The temperature measured inside Strokkur on the 20th of June 2018 (Figure 6) shows constant oscillations. It swings between 93.4°C and 106.8°C, with a average value of 100°C at 9 m depth, whereas at 16 m depth it oscillates between 102.7°C and 119.1°C, with an averaged value of 113°C (Figure 6). These values are comparable to those measured by Walter et al. (2018) who observed that between about 7 and 12 m depth the temperature is around 100°C, whereas temperatures above 110°C were found below 15 m. The amplitude of temperature variations is larger at 16 m (up to 15°C) than at 9 m depth (up to 12°C) (Figure 6). While recording temperature measures, we visually surveyed the eruptive cycle of Strokkur (Collignon et al., submitted). Comparing visual inspection and temperature data suggest that eruption occurs immediately after the maximum temperature is reached in the conduit. Eruptions cycles in Figure 6a,b can thus be defined between

two main temperature maxima, with a discharge phase characterised by a rapid decrease of the temperature after the eruption and a recharge phase, where the temperature increases more slowly (Figure 6a). The larger the temperature drop the longer is the recharge phase. This observation is consistent with Eibl et al. (2020) who observe a linear increase of the time after eruption.

While the maximum temperature preceding the eruption is reached within a few seconds at 9 m and 16 m depth inside Strokkur's conduit, the discharge phase, whose end is characterised by the local minimum temperature, is longer (up to 90 s) at shallower depths (Figure 6b). During the recharge phase temperature climbs up with an oscillatory behaviour that is more marked at depth (Figure 6b). The spectrograms of the temperature recorded at 16 m depth were obtained after detrending the data and normalising them by the absolute maximum. The changes in power/frequency spectra over time indicate that the periodicity of Strokkur changes over time. Three main dominant frequency ranges can be observed on the spectrograms (Figure 6c,d). The lowest dominant frequency is observed between 1 and 2 mHz, and its power increases between 1.4 and 2 hours (Figure 6d). This time period coincides with the occurrence of large temperature variations between 2h46 and 3h26. A second dominant frequency is observed between 4 and 5 mHz and is consistent with the periodicity of the eruptions, marked by the highest temperature. Finally, a weak frequency can be observed around 35-45 mHz. A similar spectrogram is obtained when plotting temperature recorded at 9 m inside Strokkur's conduit but it is not shown here to avoid redundancy. On the 23rd of June 2018, the temperature at ca. 10 m depth inside Strokkur varies between 96.6°C and 112.6°C, with an averaged value of 106.8°C. The temperature measured simultaneously at ca. 5 m depth inside Great Geysir's conduit also shows some periodicity even if it is less pronounced than for Strokkur. Temperature oscillates between 73°C and 76.7°C. The spectrograms of the temperatures of Great Geysir (Figure 8a, c) and Strokkur(Figure 8b, d) show a dominant frequency at around 1-2 mHz. This peak frequency is more pronounced between 1.5h and 2.5h for Great Geysir. For Strokkur this occurred between 1h and 1.5h and between 2h and 3h and coincided with the occurrence of multiple eruptions (sensu Eibl et al. (2020)). Cross-wavelet and wavelet coherence analysis also could be performed Henderson09 to compare in details the temperature signals of Great Geysir and Strokkur. However, such a study is out of the scope of the current paper.

5 Discussion

Interpreting the data collected and inverted in this study is challenging as the subsurface is characterised by a complex porous media where weathered lithological units hosting a two-phases groundwater system are offset by faults. Previous electrical acquisitions conducted in active hydrothermal systems either focused on the very large scale using magnetotelluric methods (e.g. Peacock et al. (2020)) or on the local scale using cabled geoelectrical equipment (e.g. Byrdina et al. (2014)). Only recent studies in high-enthalpy hydrothermal settings (Troiano et al., 2019; Legaz et al., 2009; Millera et al., 2020; Gómez-Ortiz et al., 2014; Mazzini et al., 2021) acquired fully 3D electrical measurements at the meso-scale that are comparable with our investigations. The *Hhf* hosts fluids at the boiling point (possibly super-heated) at shallow depths. The phase state of the

groundwater flowing in the shallow geological units may have dramatic effects on the resistive properties of the liquid- or vapour-saturated porous media. Groundwater flow in the *Hhf* is transient and extremely vigorous as shown by the temperature swings (Figures 6 and 7). While pressure variations have no major effects on the resistive physical properties of the investigated porous media, resistivity is strongly temperature-dependent (Roberts et al., 2001). The corollary is that the resistivity of vapour-saturated units may largely differ from the resistivity of the same dry units.

The *Hhf* is hosted within rhyolite lavas also cropping out in the Laugarfjall (Figure 2). Weathered rhyolitic units are often characterised by high resistive values compatible with the ones found at depth in the *Hhf* (Figures 4 and 5). Similar values for rhyolitic units have been shown to occur at the Río Tinto, Spain (Gómez-Ortiz et al., 2014). We suggest that the highly-resistive body dipping eastwards found in the centre of the *Hhf* may be interpreted as altered rhyolitic units. The intrusion of the rhyolites may have capitalised on NNE-striking pre-existing fault structures compatible with the regional tectonic field (i.e. fractures striking N23) described by Walter et al. (2018) and Thorbjarnardóttir et al. (2020). Previous authors already pointed out the importance of pre-existing faults and geological discontinuities driving the intrusion of magmatic bodies (Lupi et al., 2020) or hydrothermal fluids (Collignon et al., 2021). Hence, we speculate that the sharp transition separating the resistive domain of the *Hhf* from the conductive domain may represent an extensional fault structure striking approximately N23. At shallow depths we record the highest resistive values in the centre of the *Hhf* (Figures 4 and 5). We propose that such high resistive values, found above the ryholitic units may represent regions hosting vapour. In particular, Figure 9 shows that Strokkur, the most active geyser of within the *Hhf* seats at the margin of this domain. Boiling waters releasing vapour may hinder the growth of vegetation. This is observed in the Western part of the *Hhf* where lack of high vegetation mimics the boundaries of the highly-resistive region (dashed black lines in Figure 9). The interpretation of this volume as a vapour-saturated reservoir would agree with Eibl et al. (2020, 2021) who suggest the occurrence of a shallow bubble trap about 13-23 m West of Strokkur and at about 25-30 m depth. Figure 4 shows that the most prominent hydrothermal features of the *Hhf* are emplaced at the margins of highly-resistive regions. We speculate that the sub-vertical intrusion of rhyolitic dikes may have created enhanced hydraulic transmissivity at the margins of such intrusions ultimately promoting the development of sub-vertical highly-fractured groundwater-filled hydrothermal conduits. Such sub-vertical groundwater-filled structures are highlighted by the chargeability data that show sub-vertical not-chargeable domains located below the hydrothermal vents (Figure 5b, c). The comparison between resistivity and induced polarization data highlights that below the two main geysers of the *Hhf* the geoelectrical data differ. Figure 5 shows that Strokkur is characterised by high-resistivity and low chargeability values. Great Geysir is characterised by lower resistivities and low chargeability values. We speculate that such variations may directly reflect the eruptive cycles of the two geysers. The high resistivity identified below Strokkur, suggested to be due to the abundant occurrence of water vapour, may promote the frequent eruptions that characterise this vent. In contrast, the lack of prominent resistivity values below Great Geysir may be due to less vapour trapped at depth and reflect the much less recurrent eruptions taking place at this vent.

The dashed lines in Figure 5f seem to suggest that Strokkur and Great Geysir may be fed by a common

groundwater reservoir at about 150 m below the ground surface. Furthermore, both geysers show an oscillatory behaviour suggesting similar processes taking place at depth. To verify whether Strokkur and Geysir may be driven by the same groundwater dynamics, we detrended the temperature data (shown in Figure 7) of each geyser. This provided the temperature variations with respect to their mean values. Then, the datasets were normalised by the absolute maximum temperature before performing a cross-correlation between both signals (Figure 10). The cross-correlation was computed for time lags between -1800 and 1800 seconds. A moving average of 30 seconds was also performed to remove the highest frequencies before applying the cross-correlation. Independently of the smoothing, there were no significant peaks in the cross-correlograms and the coefficients remain low (< 0.2). This suggests that despite the qualitative observations that may suggest some sort of synchronous temperature variations at Strokkur and Great Geysir (Figure 7), there is no statistical correlation between the temperature records of the two systems (Figure 10). Yet, a similar dominant frequency around $\sim$1 mHz is observed in both temperature signals. A possible alternative explanation is that both geysers are driven by similar processes taking place in different reservoirs (e.g. bubble traps) within the *Hhf*. This would explain the similar oscillatory behaviour of both geysers and would be compatible with the lack of statistical cross-correlation between the two datasets.

Figures 6 and 7 highlight that the charging and discharging processes taking place inside the conduits of geysers are oscillatory. This behaviour is compatible with studies showing oscillatory amplitude variations of hydrothermal tremor (Vandemeulebrouck et al., 2013; Wu et al., 2017), conduit level fluctuations (Rudolph & Sohn, 2017; Rudolph et al., 2018b) and temperature variations (Lasič, 2006). Such an oscillatory behaviour may be explained by the presence of a bubble trap. This conceptual model has been further elaborated by Wu et al. (2019) who proposed that the reservoir where vapour is exsolved and accumulated may actually rather consist in a very dense network of fractures allowing fluids to advect towards a small cavity directly connected to the sub-vertical conduit of the geyser. Our acquisition does not have the necessary resolution to image such an architecture. However, the temperature oscillations shown in Figure 6 seem to indicate the occurrence of an unstable process that progressively evolves via an initial alternation of short-scale heating and cooling of the water column. Most importantly, after the eruption, the system is cooled down more rapidly at the bottom than at the surface as shown by the lag of time occurring between the two temperature minima shown in Figure 6b. This effect may be due to a pressure drop located where the exsolution and gas expansion takes place. This sort of Venturi effect promotes a pressure gradient driving nearby colder fluids inside the plumbing system of the geyser. Alternatively, a slower cooling down at shallower depths may be explained by the continuation of rising vapour that is being exsolved in the upper part of the water column due to the post-eruptive drop of pressure.

Figure 11 shows the geological model that we propose for the *Hhf*. We postulate that the region is affected by NNE-striking fault structures focusing the upwelling of the hydrothermal fluids. This is highlighted by the alignment of the springs mapped with aerial photography (Figures 1, 9) and by the elongation of the highly resistive structures at depth. Such a fault system is compatible with the model proposed by Walter et al.

(2018) and with the regional-scale deformation kinematics shown by Hjaltadóttir (2009). At about 200 m below the ground, liquid water phase transitions into vapour and fills a fractured NNE-elongated reservoir. At the margins of such a reservoir, fluids advect along vertical pipes and feed bubble traps from which geysers erupts. These sub-vertical structures are highlighted by the regions marked by low induced polarization (Figure 5b, d). While Figure 5f seems to suggest that Strokkur and Great Geysir may be fed by a common deep reservoir, the cross-correlation of temperature signals (Figure 10) seems to suggest otherwise. For this reason we speculate that fluids upwell via a complex network of fractures and are temporarily stored in at least two distinct bubble traps, i.e. one per geyser. While it is not possible to identify a bubble trap feeding Great Geysir, our electrical data seem to suggest that the region feeding Strokkur extends down to at least 50 m below the surface (Figure 5a).

Conclusions

We acquired 3D electrical and temperature measurements across the Haukadalur hydrothermal field, Iceland. We identify two distinct resistive and conductive domains separated by a marked discontinuity. We propose that NNE-striking faults affect the region focusing fluid flow at the surface. In particular, the Strokkur and the Great Geysir geysers develop upon a major extensional fault and are fed by boiling fluids rising across subvertical conduits from a common reservoir. The temperatures measured inside the geysers show a similar oscillatory behaviour but the reservoirs do not seem to be connected across shallow communicating bubble traps. The Haukadalur hydrothermal field seems to be affected by extensional tectonics that may have favoured the emplacement of shallow intrusions heating the groundwater. Fluids phase-transition into vapour and accumulate from about 200 m depth in fractured reservoirs. Vapour-saturated regions are NNE-elongated and feed active springs, fumaroles and hot ponds. This study represent to the best of our knowledge the first electrical image in 3D of a geyser-hosting hydrothermal field.
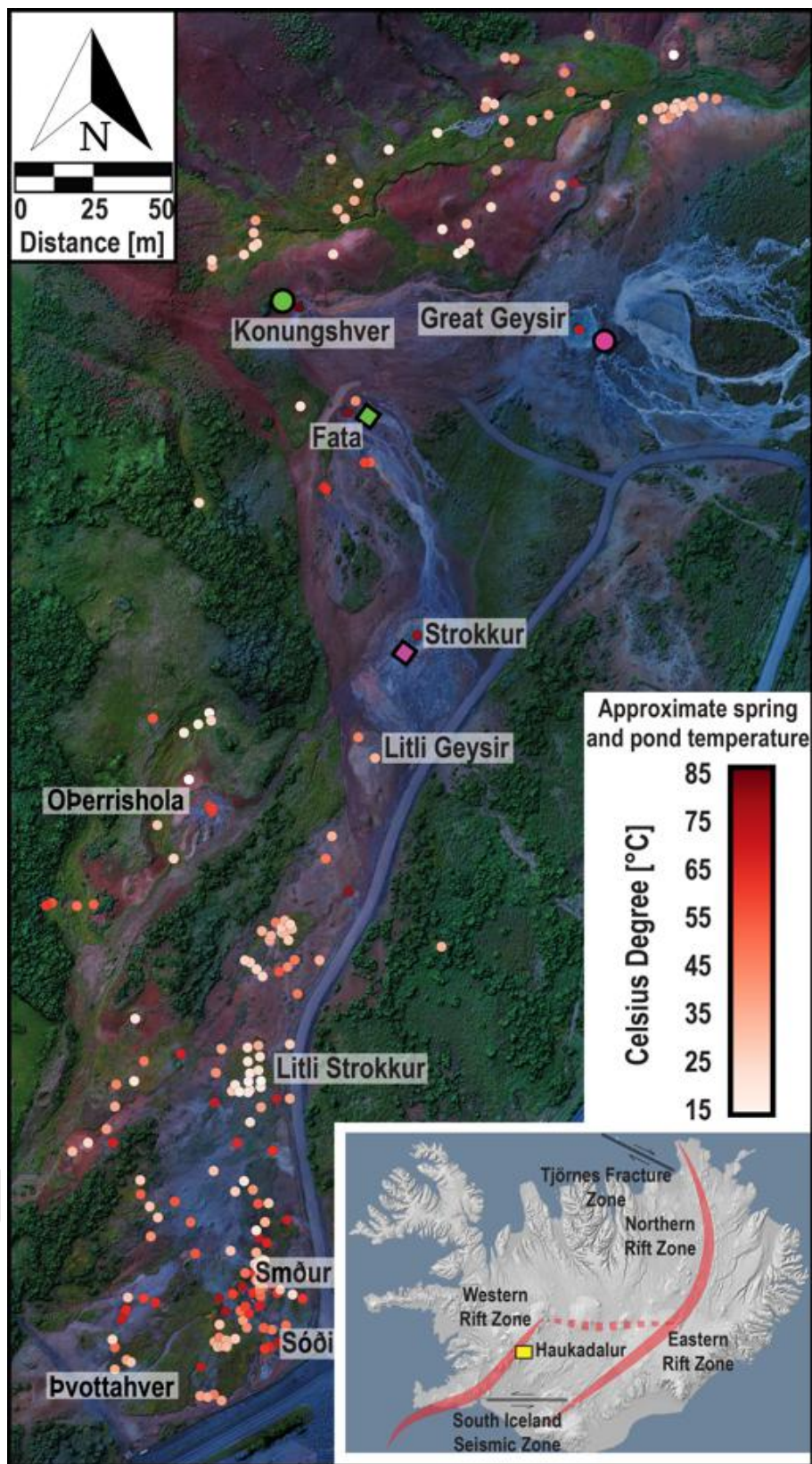
Acknowledgments

Figure 1. **Aerial view of the Haukadalur hydrothermal field and semi-quantitative temperatures of the springs and ponds.** The spring temperature varies from 15°C for some of the clusters of ponds up to 80-85°C for the Strokkur geyser and the Konungshver and Fata ponds. Temperatures are shown only to provide semi-quantitative estimate of the temperature variations across the field. These measurements have been acquired with a flir thermal camera mounted on a DJI phantom flying at 65 m above the ground. For a comparison of the uncertainty held by these measurements, Figure 6 shows that the temperature of Strokkur reaches 100°C at 9 m depth. See the main text for more details.

–13–
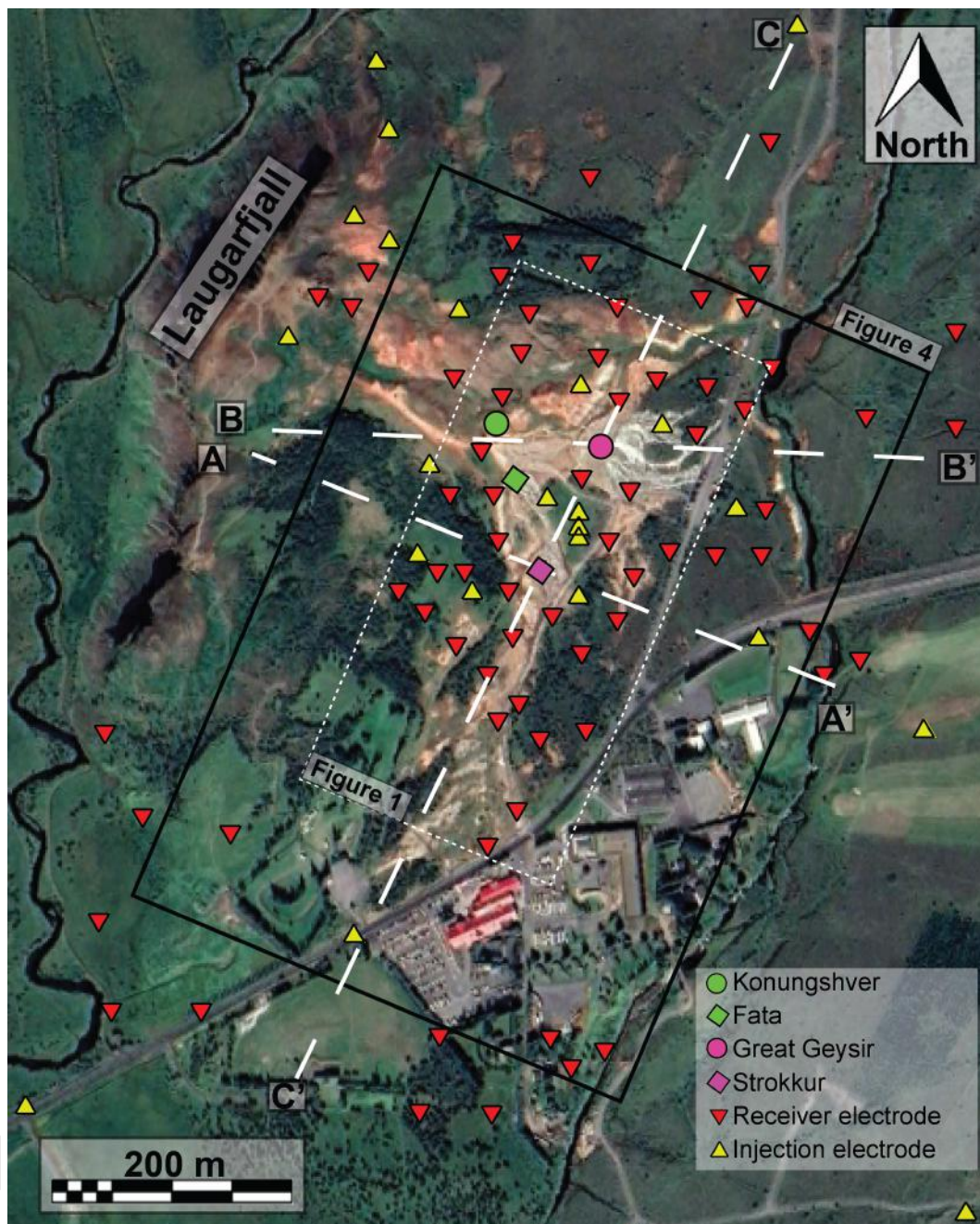
Figure 2. **Distribution of the Fullwavers across the Haukadalur hydrothermal field, Iceland.** Red triangles pointing downwards show the location of the receiving electrodes while the yellow triangles show the position of the injecting electrodes. Note that 3 more injections (2 to the North and one to the South) are falling outside the figure. For each of the 24 fullwavers, the two dipoles-dipoles were distributed in a L-shape configuration when possible. The dotted white rectangle shows the area covered in Figure 1 and the black rectangle frames the region shown in Figure 4. The dashed lines indicate the orientation of the cross section of Figure 5. The pink circle and the pink diamond show the positions of Great Geysir and Strokkur geysers, respectively. The Green circle and the green diamond show the location of Konungshver and Fata emission centres, respectively.

–14–
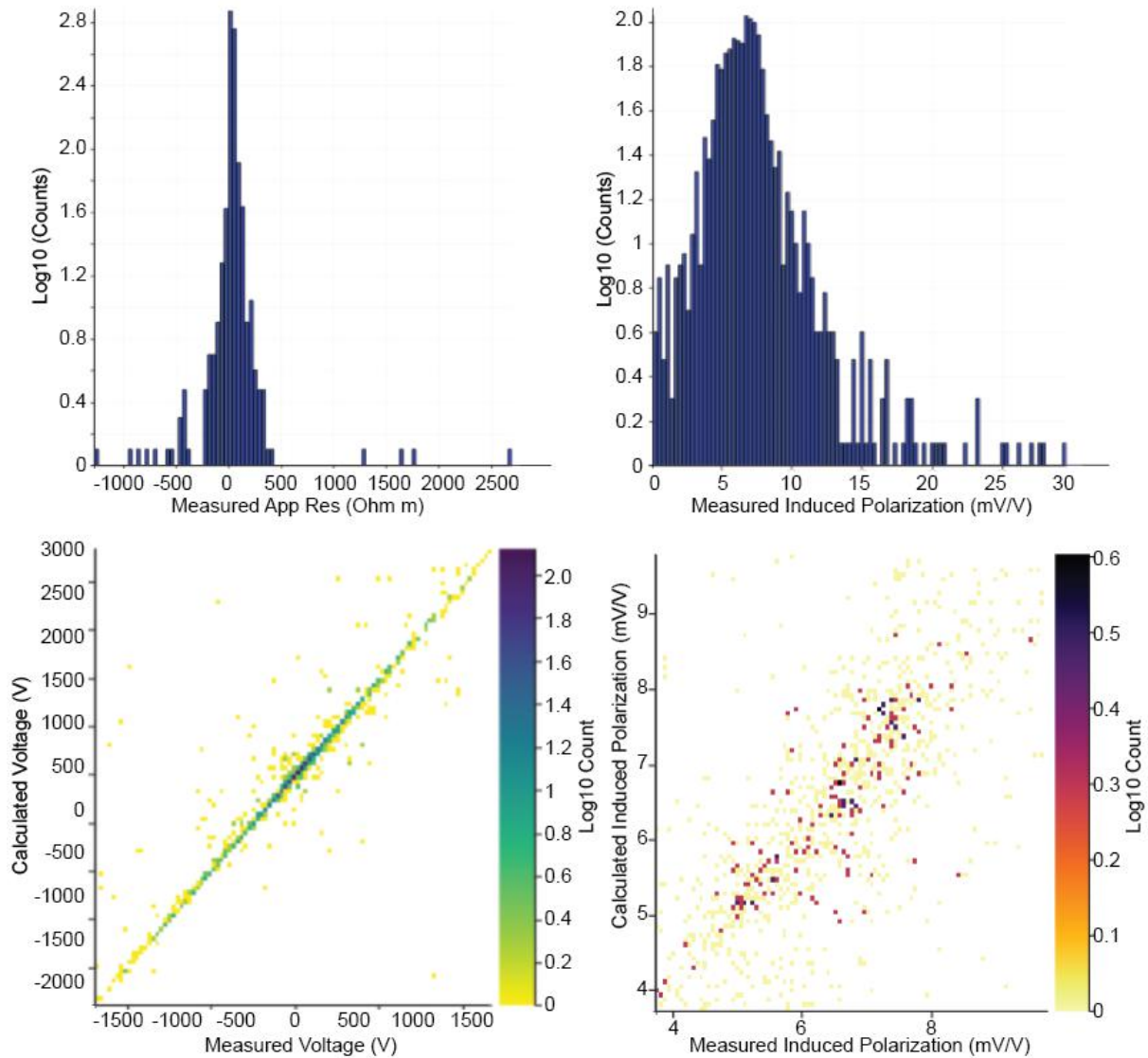
Figure 3.   Data overview. A) Apparent resistivity and B) induced polarization (chargeability) measurements. Note that the negative apparent resistivites are not related to errors during deployment but to sharp resistive contrasts at depth. C) Cross-plot for the resistivity data and for D) the induced polarization (chargeability) data.
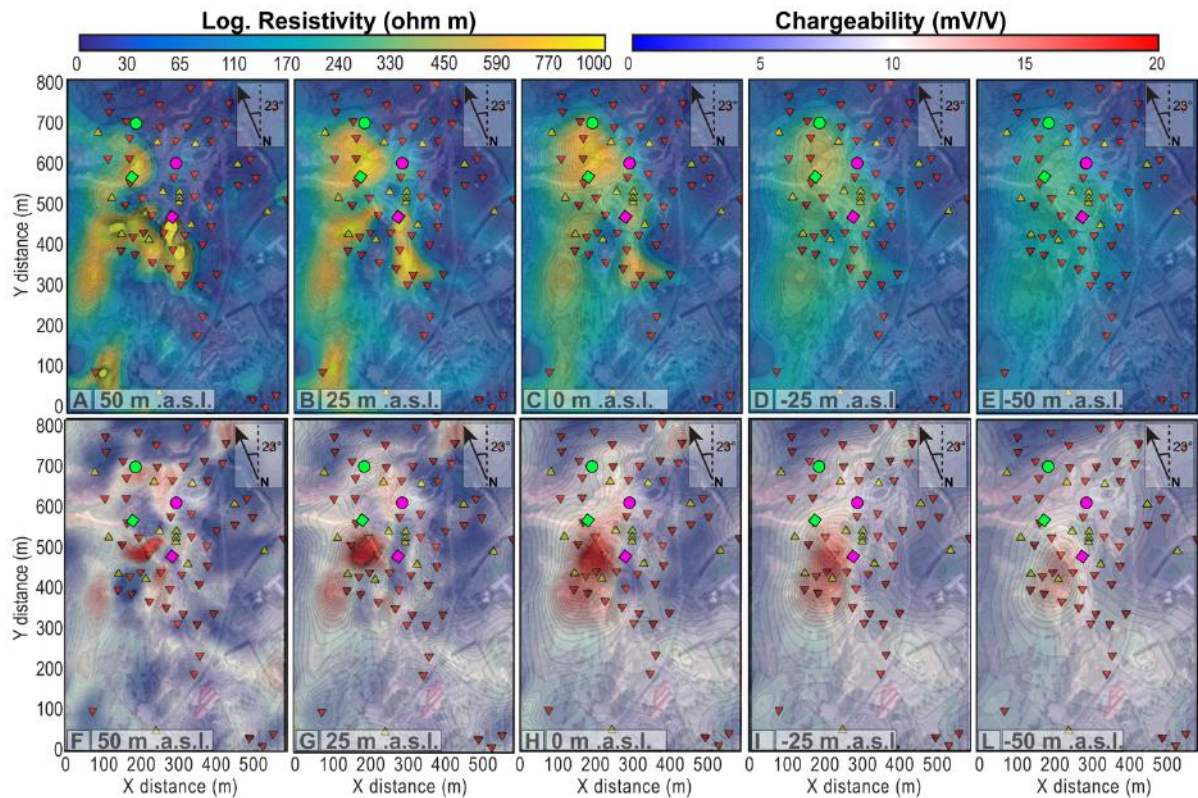
Figure 4. Horizontal slices of the inverted 3D resistive and IP models. The pink circle, pink diamond, green circle and green diamond show the locations of the Great Geysir, Strokkur, Konungshver and Fata, respectively, that are the hydrothermal emissions marked by higher temperatures (see Figure 1). The triangles show the position of the electrodes (yellow and red triangles show the positions of injecting and receiving electrodes, respectively). The limit between conductive and resistive regions seem to broadly correspond to the limit between chargeable and non-chargeable domains, see panels below 0 m a.s.l. Note that all the chargeability computations are done on integral chargeability and not chargeability sensu-stricto.
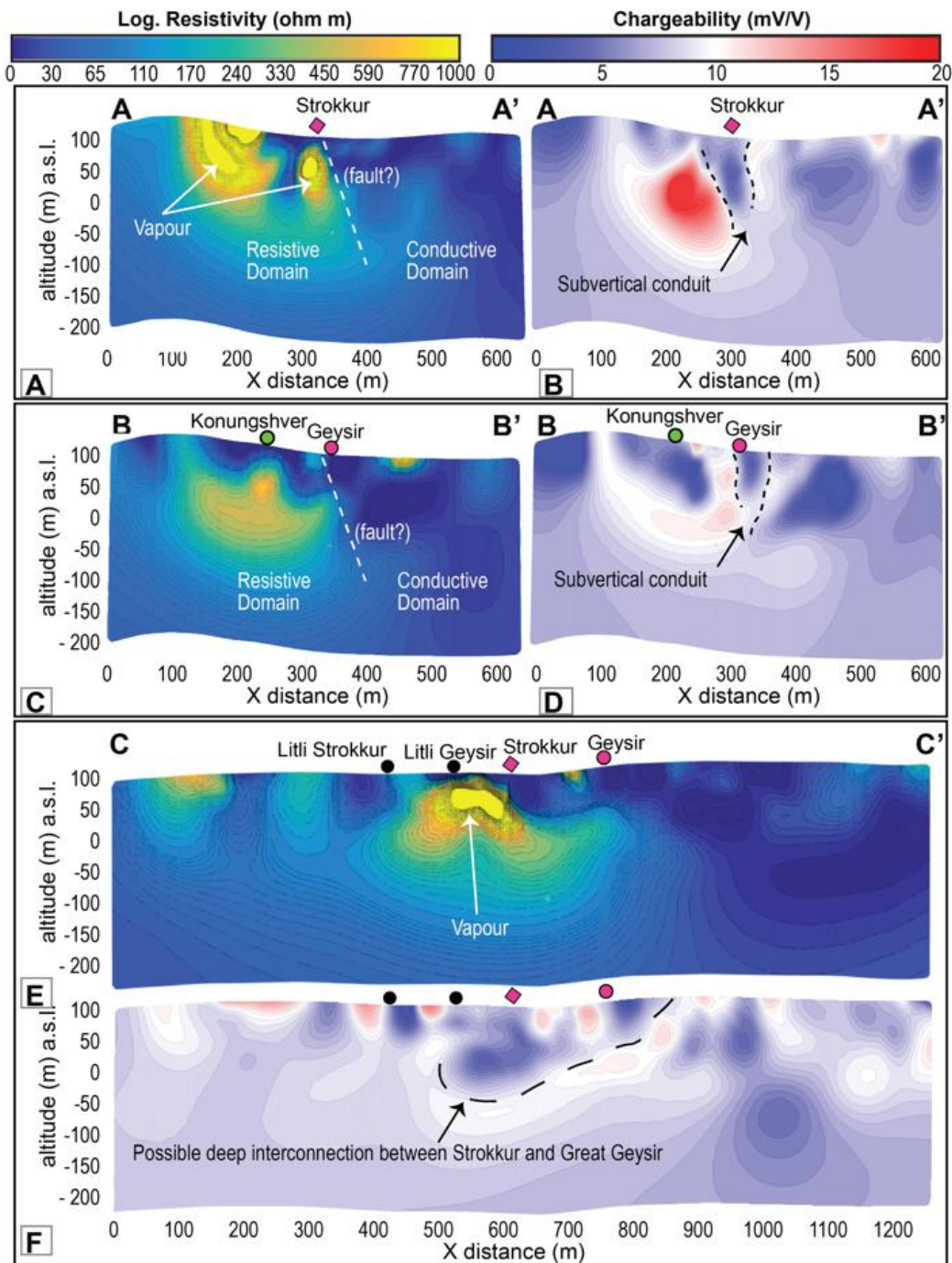
Figure 5. **Cross sections across the Haukadalur hydrothermal field.** The cross sections show the spatial relationships between various hydrothermal manifestations across the field. The vertical dashed line in panels A and B represents the limit between the resistive and conductive domains that we interpret as a fault system, discussed in Figure 9 and proposed in Figure 11.
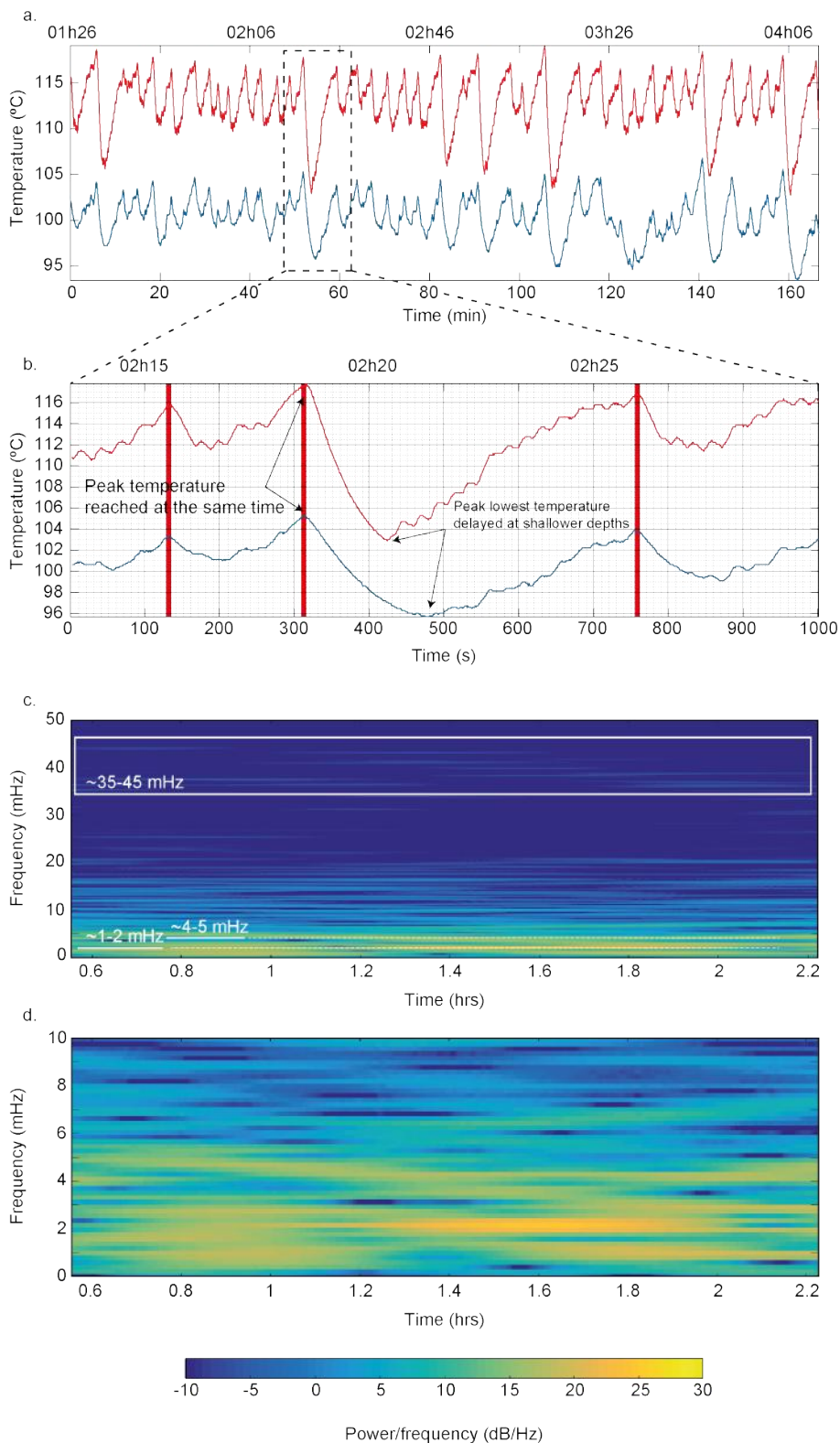
Figure 6. **Oscillatory temperature behaviour inside Strokkur geyser.** A) Temperature recorded at 9 m (blue) and 16 m (red) depth inside Strokkur's conduit during the night of 20th June 2018. B) Close view of the temperature evolution during two eruptive cycles. Vertical red bars show eruption. C) and D) Spectrograms of the temperature data (detrented and normalised) shown in panel A).
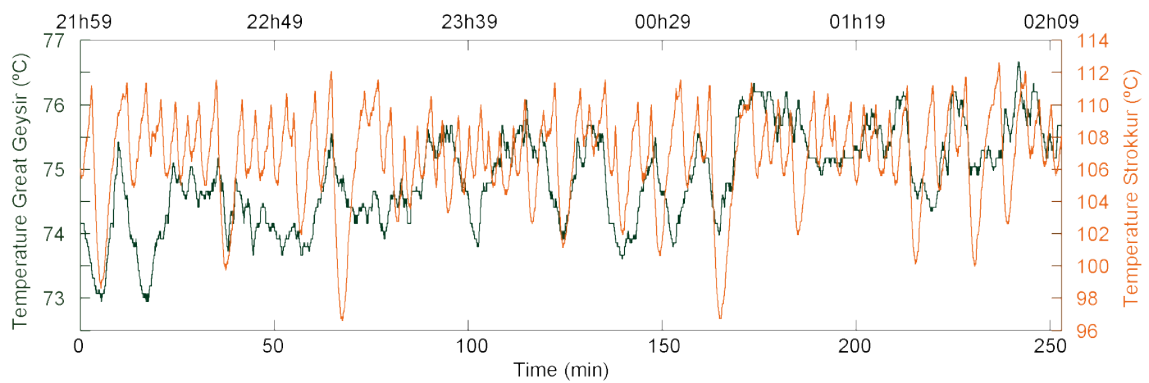
Figure 7. Temperature comparison inside Strokkur and Great Geysir. Temperature recorded at ∼5 m inside Great Geysir's (green) conduit and at ∼10 m inside Strokkur's (orange) conduit, on the 23rd June 2018.
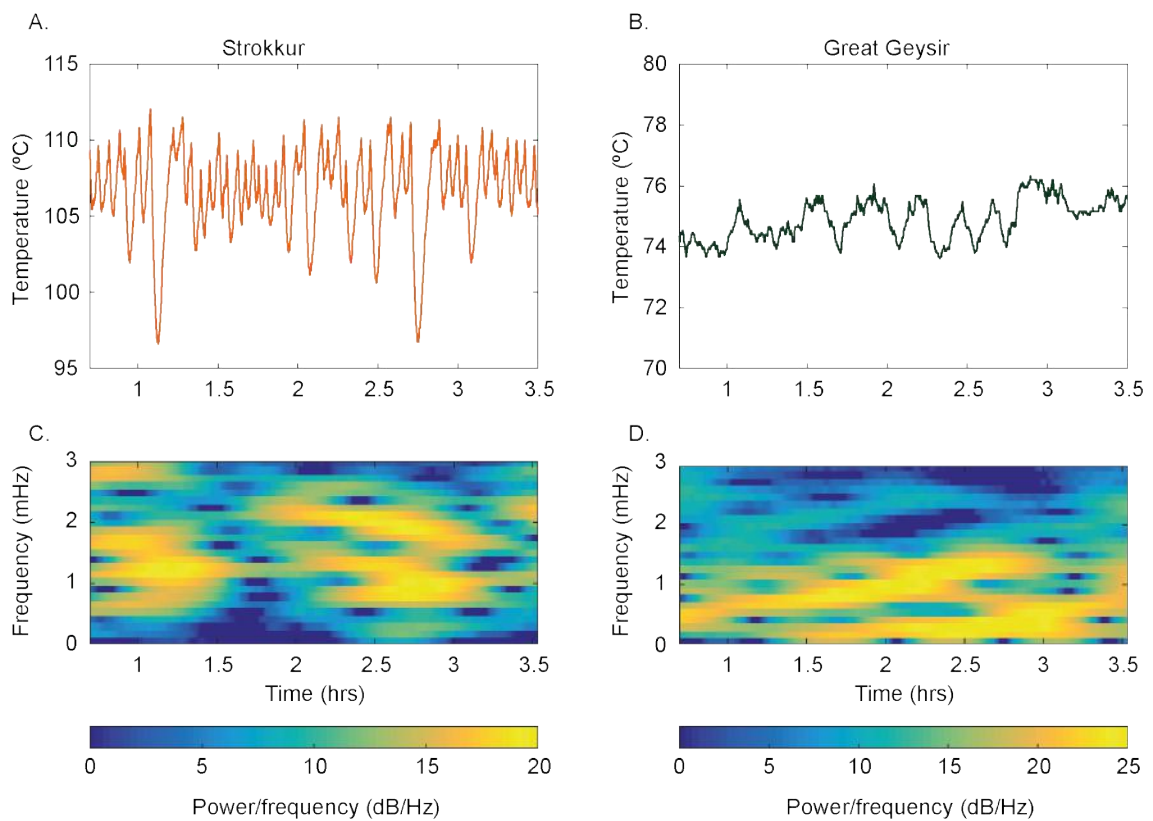

Figure 8. Periodicity of Strokkur and Great Geysir temperature signals A) Strokkur and B) Great Geysir temperature recorded on the 23rd June 2018. Spectrograms of detrented and normalised (by its absolute maximum) temperature signals of C) Strokkur and D) Great Geysir, shown in panels A and B, respectively.
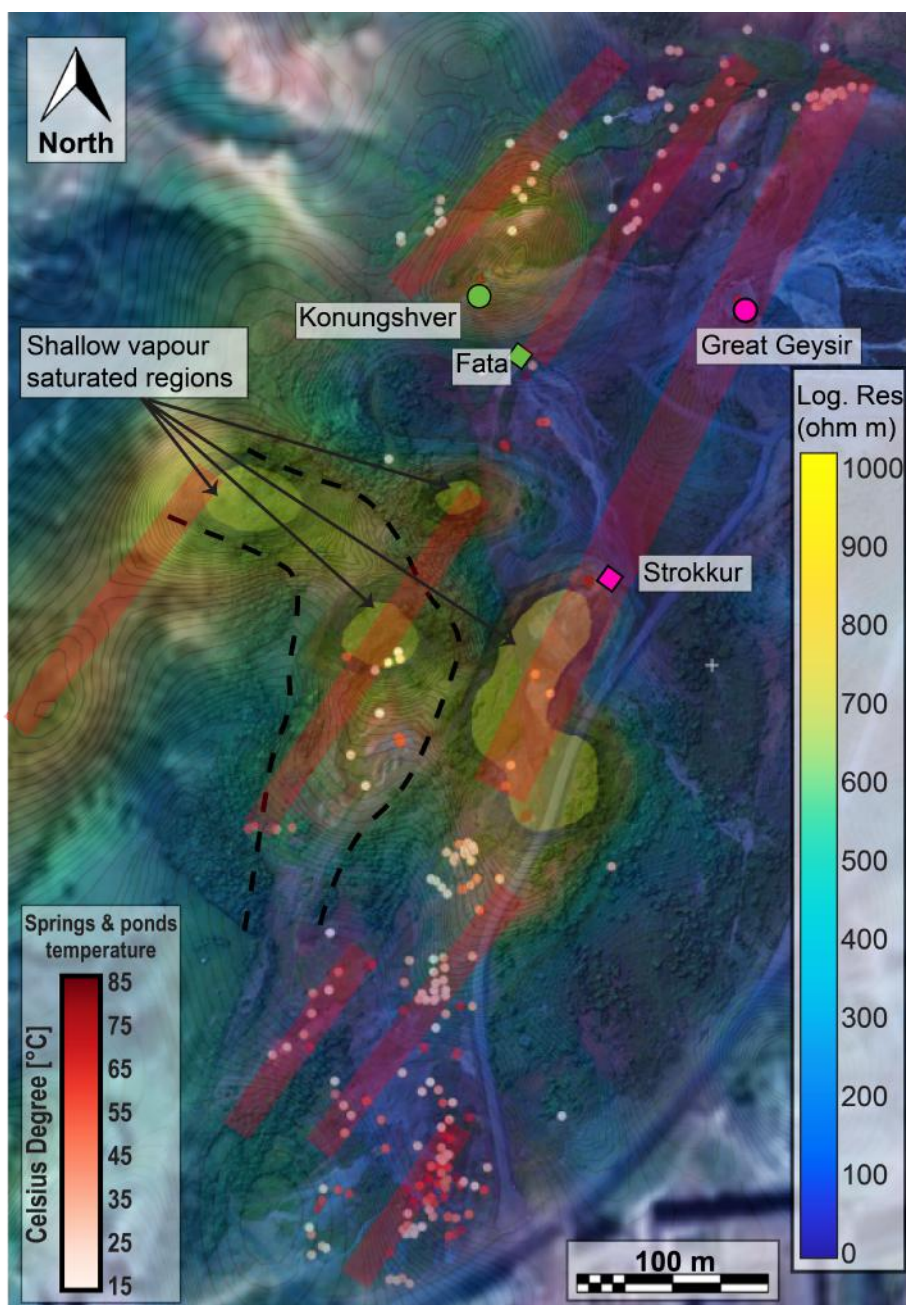
Figure 9. **Alignment of springs and hot ponds in the Hakadarul hydrothermal field.** The resistive data (the horizontal slice is 50 m below the ground) show the occurrence of high values (saturated at 1000 Ohm.m but reaching up to 12000 Ohm.m) elongated NNE-SSW. The anomaly on the East also shows a similar trend. Furthermore, the qualitative tracing of the fumaroles and hydrothermal ponds mapped with the drone seem to suggest a NNE-striking (red banded lines). The direction of these features is in agreement with the strike of the transtensional structures at the regional (Hjaltadóttir, 2009) and at the local scale (Walter et al., 2018). Furthermore, a sharp transition striking NNE-SSW is also highlighted in Figure 4d, e.
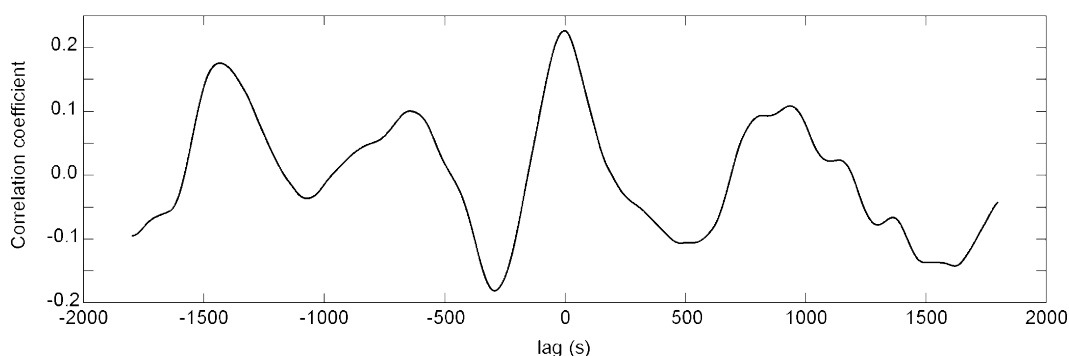
Figure 10. **Cross-correlogram between temperature variations of the Strokkur and Great Geysir geysers.** Temperature data were smoothed with a 30 s moving average, detrended and normalised by the absolute maximum before to perform the cross-correlation. Original data in Figure 7
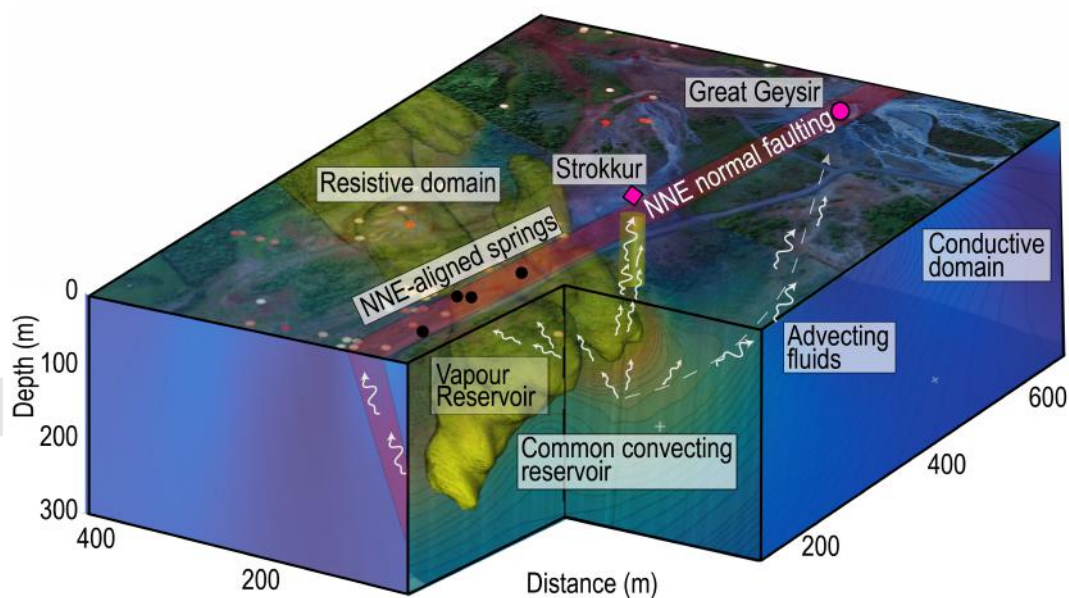
Figure 11. **Conceptual model of the Haukadarul hydrothermal field.** A NNE-striking fault system is proposed to separate the resistive and the conductive regions of the *Hhf*. The springs and hot ponds crop out along this main direction suggesting a strong control of the local tectonics on the fluid distribution at the surface. Highly-resistive regions represent geological domains charaterised by the occurrence of vapour. From here, fluids migrate upwards to feed the eruptive activity of the hydrothermal systems of the *Hhf*.

References

Adelstein, E., Tran, A., Saez, C. M., Shteinberg, A., & Manga, M. (2014). Geyser preplay and eruption in a laboratory model with a bubble trap. *Journal of Volcanology and Geothermal Research*, *285*, 129–135.

Ardid, A., Vera, E., Kelly, C., Manga, M., Munoz-Saez, C., Maksymowicz, A., & Ortega-Culaciati, F. (2019). Geometry of geyser plumbing inferred from ground deformation. *Journal of Geophysical Research: Solid Earth*, *124*(1), 1072–1083.

Barker, R. D. (1989). Depth of investigation of collinear symmetrical four-electrode arrays. *GEOPHYSICS*, *54*(8), 1031-1037.

Belousov, A., Belousova, M., & Nechayev, A. (2013). Video observations inside conduits of erupting geysers in kamchatka, russia, and their geological framework: Implications for the geyser mechanism. *Geology*, *41*(4), 387–390.

Bunsen, R. (1847). Ueber den innern zusammenhang der pseudovulkanischen erscheinungen islands. *Justus Liebigs Annalen der Chemie*, *62*(1), 1–59.

Byrdina, S., Vandemeulebrouck, J., Cardellini, C., Legaz, A., Camerlynck, C., Chiodini, G., ... others (2014). Relations between electrical resistivity, carbon dioxide flux, and self-potential in the shallow hydrothermal system of solfatara (phlegrean fields, italy). *Journal of volcanology and geothermal research*, *283*, 172–182.

Carrier, A., Fischanger, F., Gance, J., Cocchiararo, G., Morelli, G., & Lupi, M. (2019). Deep electrical resistivity tomography for the prospection of low-to medium-enthalpy geothermal resources. *Geophysical Journal International*, *219*(3), 2056–2072.

Collignon, M., Cardellini, C., Duprat-Oualid, S., Hammer, Ø., Chiodini, G., Vandemeulebrouck, J., ... Ruch, J. (2021). Carbon dioxide diffuse emission at the tolhuaca hydrothermal system (chile) controlled by tectonics and topography. *Journal of Volcanology and Geothermal Research*, *417*, 1-17.

Cros, E., Roux, P., Vandemeulebrouck, J., & Kedar, S. (2011). Locating hydrothermal acoustic sources at old faithful geyser using matched field processing. *Geophysical Journal International*, *187*(1), 385–393.

Eibl, E. P., Hainzl, S., Vesely, N. I., Walter, T. R., Jousset, P., Hersir, G. P., & Dahm, T. (2020). Eruption interval monitoring at strokkur geyser, iceland. *Geophysical Research Letters*, *47*(1), e2019GL085266.

Eibl, E. P., Müller, D., Walter, T. R., Allahbakhshi, M., Jousset, P., Hersir, G. P., & Dahm, T. (2021). Eruptive cycle and bubble trap of strokkur geyser, iceland. *Journal of Geophysical Research: Solid Earth*, *126*(4), e2020JB020769.

Gómez-Ortiz, D., Fernández-Remolar, D. C., Granda, Á., Quesada, C., Granda, T., Prieto-Ballesteros, O., ... Amils, R. (2014). Identification of the subsurface sulfide bodies responsible for acidity in río tinto source water, spain. *Earth and Planetary Science Letters*, *391*, 36–41.

Gresse, M., Vandemeulebrouck, J., Byrdina, S., Chiodini, G., Revil, A., Johnson, T. C., ... others (2017). Three-dimensional electrical resistivity tomography of the solfatara crater (italy): Implication for the multiphase flow structure of the shallow hydrothermal system. *Journal of Geophysical Research: Solid Earth*, *122*(11), 8749–8768.

Hjaltadóttir, S. (2009). *Use of relatively located microearthquakes to map fault patterns and estimate the thickness of the brittle crust in southwest iceland. sub-surface fault mapping in southwest iceland* (Unpublished doctoral dissertation).

Hurwitz, S., Clor, L. E., McCleskey, R. B., Nordstrom, D. K., Hunt, A. G., & Evans, W. C. (2016). Dissolved gases in hydrothermal (phreatic) and geyser eruptions at yellowstone national park, usa. *Geology*, *44*(3), 235–238.

Hurwitz, S., Kumar, A., Taylor, R., & Heasler, H. (2008). Climate-induced variations of geyser periodicity in yellowstone national park, usa. *Geology*, *36*(6), 451–454.

Husen, S., Taylor, R., Smith, R., & Healser, H. (2004). Changes in geyser eruption behavior and remotely triggered seismicity in yellowstone national park produced by the 2002 m 7.9 denali fault earthquake, alaska. *Geology*, *32*(6), 537–540.

Jones, B., Renaut, R. W., Torfason, H., & Owen, R. B. (2007). The geological history of geysir, iceland: a tephrochronological approach to the dating of sinter. *Journal of the Geological Society*, *164*(6), 1241–1252.

Ladd, B. S., & Ryan, M. C. (2016). Can co2 trigger a thermal geyser eruption? *Geology*, *44*(4), 307–310.

Lajaunie, M., Gance, J., Nevers, P., Malet, J., Bertrand, C., Garin, T., & Ferhat, G. (2019). Structure of the séchilienne unstable slope from large-scale three-dimensional electrical tomography using a resistivity distributed automated system (r-das). *Geophysical Journal International*, *219*(1), 129–147.

Lasič, S. (2006). Geyser model with real-time data collection. *European journal of physics*, *27*(4), 995.

Legaz, A., Vandemeulebrouck, J., Revil, A., Kemna, A., Hurst, A., Reeves, R., & Papasin, R. (2009). A case study of resistivity and self-potential signatures of hydrothermal instabilities, inferno crater lake, waimangu, new zealand. *Geophysical Research Letters*, *36*(12).

Lupi, M., Trippanera, D., Gonzalez, D., D'amico, S., Acocella, V., Cabello, C., . . . Tassara, A. (2020). Transient tectonic regimes imposed by megathrust earthquakes and the growth of nw-trending volcanic systems in the southern andes. *Tectonophysics*, *774*, 228204.

MacKenzie, G. S. (1811). *Travels in the island of iceland.*

Mazzini, A., Carrier, A., Sciarra, A., Fischanger, F., Winarto-Putro, A., & Lupi, M. (2021). 3d deep electrical resistivity tomography of the lusi eruption site in east java. *Geophysical Research Letters*, *48*(18), e2021GL092632.

Millera, C. A., Christenson, B. W., Byrdina, S., Vandemeulebrouck, J., Brakenrig, T., Britten, K., . . . Epstein, G. (2020). Snapshot of a magmatic/hydrothermal system from electrical resistivity tomography and fumarolic composition, whakaari/white island, new zealand. *Journal of Volcanology and Geothermal Research*, 106909.

Morelli, G., & LaBrecque, D. J. (1996). Advances in ert inverse modelling. *European Journal of Environmental and Engineering Geophysics*, *1*(2), 171–186.

Munoz-Saez, C., Manga, M., Hurwitz, S., Rudolph, M. L., Namiki, A., & Wang, C.-Y. (2015). Dynamics within geyser conduits, and sensitivity to environmental perturbations: Insights from a periodic geyser in the el tatio geyser field, atacama desert, chile. *Journal of Volcanology and Geothermal Research*, *292*, 41–55.

Namiki, A., Muñoz-Saez, C., & Manga, M. (2014). El cobreloa: A geyser with two distinct eruption styles. *Journal of Geophysical Research: Solid Earth*, *119*(8), 6229–6248.

O'Hara, K. D., & Esawi, E. (2013). Model for the eruption of the old faithful geyser, yellowstone national park. *GSA Today*, *23*(6), 4–9.

Pasvanoglu, S., Kristmannsdóttir, H., Björnsson, S., & Torfason, H. (1998). *Geochemical study of the geysir geothermal field in haukadalur, s-iceland.* United Nations University.

Peacock, J. R., Earney, T. E., Mangan, M. T., Schermerhorn, W. D., Glen, J. M., Walters, M., & Hartline, C. (2020). Geophysical characterization of the northwest geysers geothermal field, california. *Journal of Volcanology and Geothermal Research*, 106882.

Pollock, D., & Cirpka, O. A. (2012). Fully coupled hydrogeophysical inversion of a laboratory salt tracer experiment monitored by electrical resistivity tomography. *Water Resources Research*, *48*(1).

Pucci, S., Civico, R., Villani, F., Ricci, T., Delcher, E., Finizola, A., ... others (2016). Deep electrical resistivity tomography along the tectonically active middle aterno valley (2009 l'aquila earthquake area, central italy). *Geophysical Journal International*, *207*(2), 967–982.

Revil, A., Johnson, T., & Finizola, A. (2010). Three-dimensional resistivity tomography of vulcan's forge, vulcano island, southern italy. *Geophysical Research Letters*, *37*(15).

Roberts, J. J., Duba, A. G., Bonner, B. P., & Kasameyer, P. W. (2001). The effects of capillarity on electrical resistivity during boiling in metashale from scientific corehole sb-15-d, the geysers, california, usa. *Geothermics*, *30*(2-3), 235–254.

Rudolph, M. L., & Sohn, R. A. (2017). A model for internal oscillations in geysers, with application to old faithful (yellowstone, usa). *Journal of Volcanology and Geothermal Research*, *343*, 17–24.

Rudolph, M. L., Sohn, R. A., & Lev, E. (2018a). Fluid oscillations in a laboratory geyser with a bubble trap. *Journal of Volcanology and Geothermal Research*, *368*, 100–110.

Rudolph, M. L., Sohn, R. A., & Lev, E. (2018b). Fluid oscillations in a laboratory geyser with a bubble trap. *Journal of Volcanology and Geothermal Research*, *368*, 100–110.

Sapia, V., Villani, F., Fischanger, F., Lupi, M., Baccheschi, P., Pantosti, D., ... others (2021). 3-d deep electrical resistivity tomography of the major basin related to the 2016 mw 6.5 central italy earthquake fault. *Tectonics*, *40*(4), e2020TC006628.

Thorbjarnardóttir, B. S., Bjarnason, I. T., & Parameswaran, R. M. (2020). The great geysir and tectonic interactions in south iceland. *American Journal of Science*, *Online, 4–8 May 2020, EGU2020-16388*.

Torfason, H., & Davíðsson, I. (1985). *The great geysir.* geysir conservation committee.

Troiano, A., Isaia, R., Di Giuseppe, M. G., Tramparulo, F. D., & Vitale, S. (2019). Deep electrical resistivity tomography for a 3d picture of the most active sector of campi flegrei caldera. *Scientific reports*, *9*(1), 1–10.

Vandemeulebrouck, J., Roux, P., & Cros, E. (2013). The plumbing of old faithful geyser revealed by hydrothermal tremor. *Geophysical Research Letters*, *40*(10), 1989–1993.

Vandemeulebrouck, J., Sohn, R. A., Rudolph, M. L., Hurwitz, S., Manga, M., Johnston, M. J., ... others (2014).

Eruptions at lone star geyser, yellowstone national park, usa: 2. constraints on subsurface dynamics. *Journal of Geophysical Research: Solid Earth*, *119*(12), 8688–8707.

Walter, T. R., Jousset, P., Allahbakhshi, M., Witt, T., Gudmundsson, M. T., & Hersir, G. P. (2018). Underwater and drone based photogrammetry reveals structural control at geysir geothermal field in iceland. *Journal of Volcanology and Geothermal Research*.

Wu, S.-M., Lin, F.-C., Farrell, J., & Allam, A. (2019). Imaging the deep subsurface plumbing of old faithful geyser from low-frequency hydrothermal tremor migration. *Geophysical Research Letters*, *46*(13), 7315–7322.

Wu, S.-M., Ward, K. M., Farrell, J., Lin, F.-C., Karplus, M., & Smith, R. B. (2017). Anatomy of old faithful from subsurface seismic imaging of the yellowstone upper geyser basin. *Geophysical Research Letters*, *44*(20), 10–240.